International Journal of Mechanical Sciences 238 (2023) 107826

Contents lists available at ScienceDirect

International Journal of Mechanical Sciences

journal homepage: www.elsevier.com/locate/ijmecsci

Analysis of the oscillations induced by a supersonic jet applied to produce nanofibers

F. Quintero [a,b,*], A.F. Doval [b], A. Goitia [a], R. Vázquez [c], K. Crespo [c], R. Barciela [a,b], M. Fernández-Arias [a,b], F. Lusquiños [a,b], A. Otto [c], J. Pou [a,b]

[a] CINTECX, LaserON Research Group, Universidade de Vigo, Vigo 36310, España
[b] Applied Physics Department, E.E.I., Universidade de Vigo, Vigo 36310, España
[c] Institute of Production Engineering and Photonic Technologies, Technische Universität Wien, Vienna 1060, Austria

ARTICLE INFO

Keywords:
Cofiblas
Nanofiber
Melt blowing
Supersonic nozzle
Flow visualization

ABSTRACT

High-performance fibers are key components for enhancing the mechanical properties of composite materials. The development of high strength nanofibers augurs the production of new nano-composites with outstanding features. However, the robust production of continuous glass nanofibers that can be feasible processed for efficiently manufacturing nanocomposites is still challenging. Recently, Cofiblas (Continuous Fiberizing by Laser melting and Supersonic dragging) was demonstrated as a technique capable of producing continuous glass nanofibers with unlimited length. Cofiblas process has some similarities with the widely known melt blowing technique for the production of polymeric fibers. In both techniques, the design of the gas nozzle is key to ensure the feasibility of the process since the turbulences of the gas jet may induce strong whipping of the filament.

This paper gives novel experimental evidences on the correlation of the supersonic gas jet instabilities with the oscillation of the filament in the melt-blowing and Cofiblas processes, relating these oscillations with the presence of shock waves and unsteadiness in the flow, and gives valuable insight into the use of supersonic jets in the melt blowing process as an effective approach for the formation of nanofibers. A thin 3D-axisymmetric model in *OpenFOAM®* was put to test by comparing the performance of different solvers which were validated by flow visualization of the exit jet using digital holography (DH). In order to perform a realistic and thorough validation, we simulated the optical measurements of the flow from the CFD simulations of the mass density by Abel transform and numerical differentiation. The application of digital holography as the flow visualization technique makes possible both a precise validation of the density maps obtained from the Abel transformation of the 2D-alike results, and the analysis of the shockwave pattern in the air jet. Conversely, the numerical reconstruction of time-averaged holograms is employed to detect unsteadiness in the flow and to analyze the fiber oscillation, which is essential to assess the stability of the process. Lastly, the analysis and comparison of the vibration of the filament using the basic design and the optimized nozzle demonstrates a clear influence of the shock waves and flow unsteadiness in the stability of the filament.

1. Introduction

High-performance fibers are key components for enhancing the mechanical properties of composite materials. The discovering of the exceptional strength of carbon nanotubes, showing ultimate tensile strength and modulus in the order of 100 GPa and 1 TPa, respectively [1], stimulated great efforts during the last decades in the search for glass and polymer nanofibers with outstanding mechanical properties. It has recently been shown that silica nanofibers can achieve tensile strengths more than twice that of microfibers and elongation at failure greater than three times higher [2], while PAN (polyacrylonitrile) nanofibers attained strengths five to ten times that of microfibers [3]. These exceptional properties of nanotubes and nanofibers predicted the production of new nano-composites with exceptional mechanical properties [4,5]. However, existing nanocomposites fall short of these expectations partially because the reduced length of the nanofibers and nanotubes limits mechanical strengthening [6] and makes it difficult to

Abbreviations: CFD, computational fluid dynamics; DH, digital holography; GOP, gradient of optical phase; MLN, minimun length nozzle; MOC, method of characteristics; PISO, pressure-implicit with splitting operators; TAHR, time-averaged holographic reconstruction.

* Corresponding author at: CINTECX, LaserON Research Group, Universidade de Vigo, Vigo 36310, España.
E-mail address: fquintero@uvigo.es (F. Quintero).

https://doi.org/10.1016/j.ijmecsci.2022.107826
Received 20 May 2022; Received in revised form 6 October 2022; Accepted 6 October 2022
Available online 8 October 2022

Nomenclature

A	cross sectional area of the nozzle,
C_μ	turbulence empirical constant,
D	diameter,
e	total energy of the fluid,
I	turbulence intensity,
$J(c_1, \ldots, c_N)$	function of nozzle contour coefficients for optimization,
M	Mach number,
M_w	Molecular weight,
p	static pressure,
R	gas constant,
T	temperature,
u_i	components of the velocity vector,
U	average flow velocity,
x_i	coordinate system (in cartesian coordinates: $x_1 = x$, $x_2 = y$, $x_3 = z$),

Greek letters

α	Mach angle,
γ	specific heat ratio,
δ_{ij}	Kronecker delta,
$\Delta\phi$	change of optical phase,
ϵ	turbulence dissipation rate,
θ	angle of velocity vector with x axis,
κ	turbulence kinetic energy,
λ	laser radiation wavelength,
μ	dynamic viscosity,
ν	kinematic viscosity,
ρ	fluid density,
ω	specific dissipation rate,

Subscripts

a	Stagnation conditions,
E	Exit conditions,
I	Inlet conditions,
t	turbulent,
T	Throat conditions.

manufacture the nanocomposites without causing agglomeration or misalignment of the reinforcing phase [4]. The robust production of continuous glass nanofibers that can be feasible processed for manufacturing nanocomposites is still challenging.

Melt-spinning is the most widely used method of obtaining polymer [7] and glass fibers [8] due to its economic advantages and high production rate. For this reason, it is extensively used in industry for manufacturing ordered yarns of continuous polymer and glass fibers for multiple applications, however it's not a suitable technique for making fibers with diameters within the nanometer scale. Another widely employed technique for fiber production is electrospinning, a simple and cost-effective method that can be used with a wide range of polymers. Electrospinning can be employed to generate ordered and aligned nanofibers that can be collected as yarns or mats [9,10]. Therefore, polymer microfibers are mainly mass-produced by melt spinning (or its variants wet-spinning and dry-wet spinning), while electrospinning is the choice to produce polymer fibers of nanometer-size diameters [9]. Although the advantages of the electrospinning technique are clear, it has some limitations. Mainly, it is only possible to use it with polymers or other compounds that can melt at low temperatures, on the order of a few hundred degrees Celsius. Finally, perhaps the most relevant drawbacks of electrospinning for its extensive industrial application are its low throughput and reproducibility [9,11], as well as environmental problems resulting from the large-scale use of solvents [10].

Alternatively, melt blowing is a conventional fabrication method of polymeric micro- and nanofibers. In this process a polymer melt is extruded through small nozzles surrounded by a high speed hot gas jet which stretches the molten filament [12]. This process is routinely employed in industry to spin fibers onto a surface producing nonwoven mats for their application as filtration devices, hygienic equipment or insulation in buildings or automotive industry [13]. Although this method has been demonstrated to reach nanometric diameters of the fibers [14,15], it is still limited to the production of nonwovens of thermoplastic polymers with diameters in the range of some micrometers. In any case, these works demonstrated that the most efficient and productive approach to reduce the polymer filament down to the nanometric regime is to increase the elongational force by applying a high speed air jet which leads to thinner fibers and faster production rates. However, this approach presents some difficulties since it may cause the fiber to undergo violent oscillations (often referred as whipping in the context of melt blowing) and may also produce an unstable air flow field which is responsible for a large quantity of unbound fibers (flies) [12].

Simulations of the aerodynamic interactions of the air jet with the filament have proven to be very useful to analyze its behavior and improve the designs of polymer dies and air nozzles. The early and continued work of some groups such as the one led by Shambaugh [16–19] proposed several models of the interactions of polymeric filament with air jet. Turbulence of the air flow field was first considered in the modeling for the melt blowing process by Entov and Yarin et al. [20]. Some different groups extended this field of investigation [21–23] with the aim of improving the performance of the process. These works model the field of airflow velocities considering the flow turbulence with different models (mainly Reynolds Stress Model and κ-ε model). Recently, the work performed by Wieland et al. [24] alleged that these previous simulations underestimate the fiber elongation by several orders of magnitude. Alternatively, they proposed an stochastic model to introduce turbulence velocity and demonstrated that turbulence has a strong effect on the elongation ratio of the filament, predicting results closer to experiments. Sinha-Ray et al. [25] focused their attention on the role that turbulence played in fiber whipping. They found that the initial perturbations of the polymer filament are provoked by large turbulent eddies of the surrounding air flow. The aerodynamic lift force distributed along the filament helps to amplify the bending perturbations; meanwhile, the stretching force by air imposes restrictions on large amplitude bending. Importantly, experimental measurements of the air flow direction demonstrated that a small lateral component of the velocity has a crucial effect on initiating instability or whipping [26]; whereas, more recently, Yang et al. [27] compared different nozzle configurations to experimentally measure the turbulence intensity and Reynolds shear stress which positively related to the bending instabilities in the filament.

On the other hand, many previous works dealt with the analysis and design of the filament injection die and the air nozzle in order to reach the required high attenuation force to obtain a thin fiber and, at the same time, preventing the instabilities on the filament [27,28]. However, although the use of a high-speed jet has proven to be effective in increasing the performance of the process and obtaining finer fibers, most of these works are restricted to subsonic regime with relative low flow velocities. In fact, there are hardly a couple of works that explore the advantages of applying supersonic nozzles in this process [29,30].

Although it is evident that turbulence and supersonic features of the air flow have a notable influence on the prediction of the performance of melt blowing by high speed air jets, the work of Wieland et al. [24]

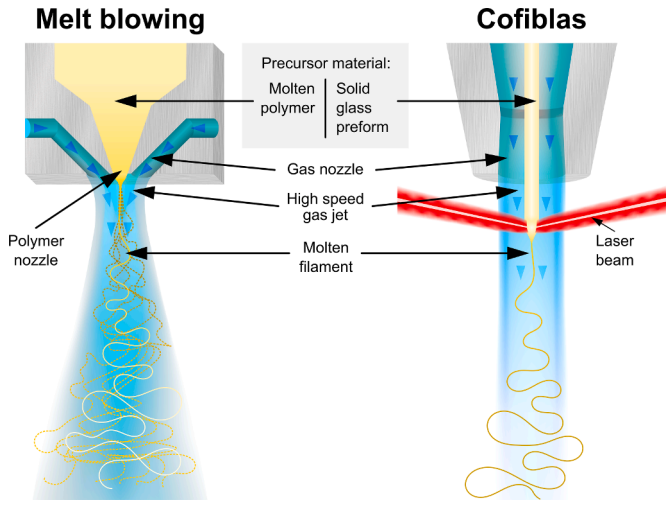

Fig. 1. Schematic representation of the melt blowing and Cofiblas processes showing their similarities and differences: both processes are based on the elongation of a fluid filament by means of a high-speed gas jet. In the case of melt-blowing, the filament is a flow of molten material (polymer or glass) extruded through a die. The gas is injected through lateral slots that converge on the filament. The Cofiblas uses a solid glass preform that is melted by two laser beams at the nozzle exit, the gas jet is injected with a supersonic nozzle that concentrically surrounds the solid preform.

revealed, that there is still no experimental proven critical selection of the turbulence and shock wave resolution algorithms in modeling the airflow field in the melt-blowing process. Conceivably, the reason for this deficiency is due to the extreme complexity to perform experimental measurements of turbulence and supersonic phenomena in the filament domain. Recently, the group led by Yongchun Zeng introduced the two hot-wire anemometer as an effective technique to analyze the turbulence in the filament [27,31].

In short, we can conclude that the optimization of the interaction of high speed air jet with the filament is crucial to optimize the process and obtain nanofibers. And, although it is true that there are some experimental works and simulations in this sense, this is a field that has not been explored as deeply as to that dedicated to analyzing the dynamics of the filament during melt-blowing, as can be verified when comparing recent bibliographic reviews in both fields [12,28,32]. Consequently, in the judgment of the present authors, further developments on stable and supersonic air jets are required to obtain thinner fibers and to improve the stability of the melt blowing process. Very importantly, the design of the nozzles must be optimized in order to generate perfectly expanded, stable supersonic jets, since the operation of supersonic nozzles outside their exact working pressure produces an overexpanded or underexpanded jet with non-uniform lateral flow. Furthermore, the internal profile of the supersonic nozzle must be optimized to avoid the formation of oblique shock waves, which can be formed even working at the exact operation pressure provoking flow separation into the nozzle. Moreover, the presence of shock waves amplifies the turbulences in the flow [33] whereas both phenomena have a strong effect on the stability and whipping motion of the filament.

Flow visualization and measurement techniques are an invaluable aid to verify the accuracy of the simulations and check whether the actual behavior of the jet produced by a supersonic nozzle satisfies the design specifications. Optical measurement techniques are non-invasive and, therefore, can be applied without disturbing the gas flow [34]. Among these, digital holography (DH) is a particularly versatile choice that provides the high sensitivity of interferometry and, at the same time, is able to operate with non-uniform or diffuse illumination, what makes unnecessary the use of large high-quality optical elements to accommodate the field of view.

Digital holography provides quantitative measurements of a transversal projection of the mass density distribution across the gas jet. These measurements may be post-processed by using tomographic techniques to get the 3D mass density distribution inside the jet, or by numerical differentiation to highlight features related to the gradient of the mass density, such as the shock waves. In addition, long exposure time-averaged holograms are affected by instability and vibration and can be used to identify regions of unsteady flow and turbulence as well as to detect the oscillation of elements as, in the present application, the glass filament.

The purpose of this paper is to present the analysis on how different supersonic flows affect to the filament oscillation. The paper first presents the design of the first generation supersonic nozzle employed to stretch a laser melted glass filament using the novel and original Cofiblas technique [35]. The Cofiblas technique was developed by some of the present authors as an evolution of the Laser Spinning technique [36,37] to achieve the continuous production of glass nanofibers. More recently, a similar method called laser-assisted melt-blown (LAMB) has been proposed for the production of polypropylene nanofibers [38]. In our previously published works on the Cofiblas a simple "first generation" supersonic nozzle was used. The present work presents an analysis of the performance of this nozzle using numerical simulation together with flow visualization by digital holography. An evaluation of three different solvers was performed by comparing with the optical measurements of the flow, allowing to model the subsonic, transonic, and supersonic regimes of turbulent viscous flows. The analysis of the first nozzle served to select the best algorithm for the simulation and to identify the defects of the original design of the nozzle profile. The outcomes from the analysis of the first nozzle supported the design of a second generation nozzle which was optimized with the help of flow simulation and verified by flow visualization. The analysis with digital holography allows to examine the development of shock waves and flow unsteadiness, and to give novel experimental evidences on the correlation of the supersonic instabilities in the flow with the oscillation of the filament in the melt-blowing and Cofiblas processes. The use of high-pressure air jets in the melt blowing process is restricted by the strong whipping that they induce, however we demonstrate that it can be avoided by using an optimized supersonic nozzle. This piece of work gives valuable insight into the use of supersonic jets in the melt blowing process as an effective approach for the formation of nanofibers.

2. Nozzles design

The original design of the supersonic coaxial nozzle specifically developed for the Cofiblas process is described in this section. First, the Cofiblas process is presented in comparison with the conventional melt-blowing mainly employed for polymers. Then, a detailed description of a basic nozzle design is presented. After the presentation of the design of the basic nozzle based in the one-dimensional dynamic theory, which yields a profile composed of cylindrical and frustoconical surfaces, we present the procedure used to apply the method of characteristics in order to design an optimized nozzle profile.

The nozzles analyzed and presented in this work were designed as a key element of a new method capable of producing individual glass nanofibers in a stable and continuous manner: the Cofiblas (Continuous Fiberizing by Laser melting and Supersonic dragging) [35]. This novel method bears many similarities to the melt blowing process: it uses a supersonic nozzle to generate a high-speed flow which drags and stretches a preform that is concurrently heated by a CO_2 laser (see Fig. 1). The exit flow generated by the nozzle needs to be stable and free of shock waves not to break the fiber in its more fragile state of fusion. The design of the nozzle shape is key to obtain the optimal conditions of the exit flow. Therefore, the outcomes of the present work can be very useful for the design of supersonic nozzles in the melt blowing process.

The main approaches for nozzle design are the one-dimensional (1D) dynamic theory and the method of characteristics (MOC). Both methods have been used for years and are well documented in the literature [39].

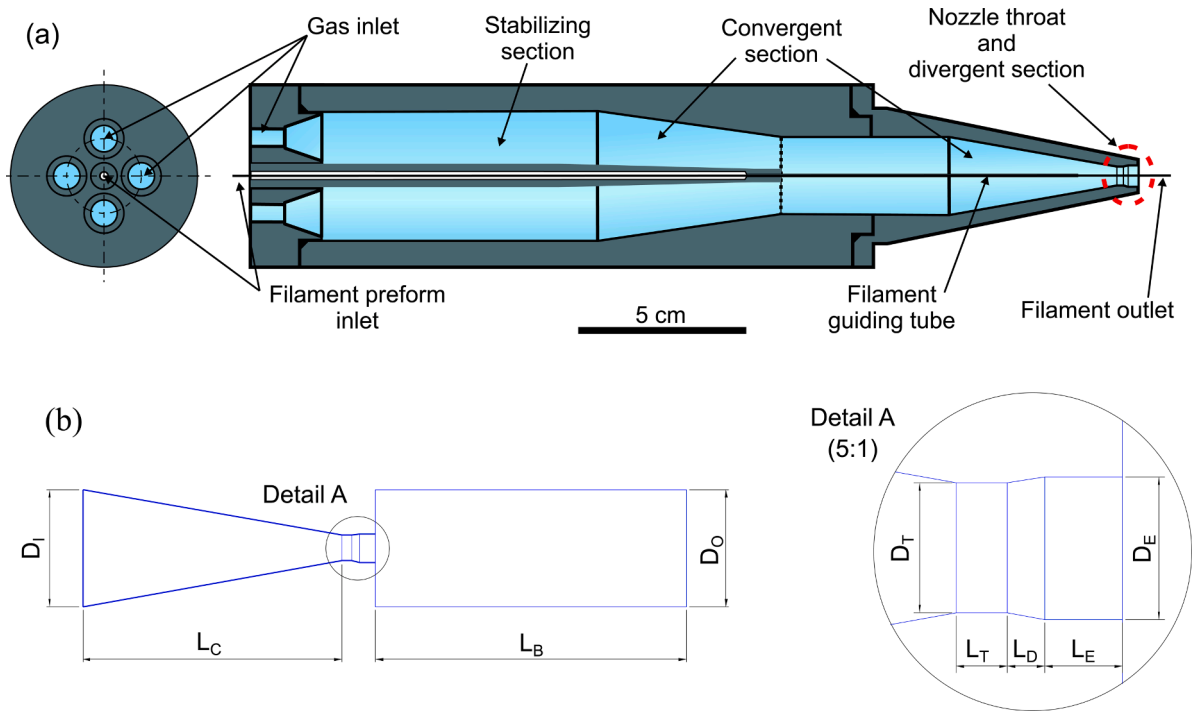

Fig. 2. (a) Full geometry of the basic design of the nozzle, based in frustoconical sections, showing the central duct to guide the filament preform surrounded by the air nozzle conduit. This includes two cylindrical stabilizing sections to minimize turbulences, two frustoconical convergent sections to progressively reduce the cross-section, and the supersonic part comprising the nozzle throat, the frustoconical divergent section, and the cylindrical exit section with diameter of 5.5 mm. (b) Reduced proposed nozzle geometry for improving computational speed. It includes just the last convergent section, the nozzle throat and divergent section and a part of the free jet with length L_B.

One dimensional theory allows the estimation of habitual parameters (e.g., pressure, velocity, Mach number, etc.). For a 1D compressible flow analysis, some assumptions had to be contemplated:

- nearly one-dimensional, unidirectional flow,
- an adiabatic flow,
- low frictional losses,
- air as a perfect gas.

These assumptions make the one-dimensional theory the simplest theory to calculate optimal expansion in a nozzle employing Eqs. (1) and (2) [40]. At a given stagnation pressure using Eq. (1) is possible to compute the Mach number at the exit and with this information, the area of the exit section could be also estimated using Eq. (2).

$$M = \left\{ \frac{2}{\gamma - 1} \left[\left(\frac{p_a}{p_E} \right)^{\frac{\gamma-1}{\gamma}} - 1 \right] \right\}^{\frac{1}{2}} \tag{1}$$

$$\frac{A_E}{A_T} = \frac{1}{M_E} \left(\frac{1 + \frac{\gamma-1}{2} M_E^2}{1 + \frac{\gamma-1}{2}} \right)^{\frac{\gamma+1}{2(\gamma-1)}} \tag{2}$$

whereas $\frac{p_a}{p_E}$ is the pressure ratio between stagnation pressure p_a and exit pressure p_E. Since the nozzle is aimed to work in the supersonic regime with a Mach number of 1,46, it means a supersonic regime, a non-linear effect (e.g., shockwaves) should be considered. In order to avoid this non-linear phenomenon and to reach an ideal expansion of the nozzle, the exit pressure p_E was set as the atmospheric pressure. M_E is the exit Mach number and the $\frac{A_E}{A_T}$ represents the area ratio between exit area A_E and throat area A_T.

The Fig. 2a shown below presents the first nozzle design derived from the 1D equations. The figure depicts a diametrical cross-section of the prototype with cylindrical symmetry. It shows the central duct to guide the filament preform surrounded by the air nozzle conduit including two stabilizing sections to minimize the multidimensional effects and turbulences, two convergent sections to progressively reduce the cross-section, and the supersonic part comprising the nozzle throat and the divergent section. The convergent sections were designed as frustoconical surfaces with small half-apex angles of 15.7° and 19.4° for the first and second sections, respectively, these angles and that of the divergent section were selected based in previous experience with similar nozzle design in order to achieve a uniform flow in the shortest possible length. The throat was included as a short cylindrical section with 5.0 mm of diameter and 2.0 mm length, while the divergent part of the nozzle is another frustoconical surface with half-apex angle of 19.4° and exit section diameter of 5.5 mm. Consequently, the borders between these sections are straight edges. These dimensions were selected heuristically to house the preform guide duct and allow a sufficient, but not excessive, air flow so that the free jet generated is capable of stretching the molten filament. This basic design was carried out by calculating the outlet diameter using 1D theory, however the outlet diameter was slightly increased with respect to the results of the isentropic equations to account for the effect of viscous losses and to round the dimensions with the aim of facilitating the manufacture of the prototype.

Oblique shock waves and expansion waves are intrinsically multidimensional effects which cannot be predicted using one-dimensional models. On the other hand, the Method of characteristics (MOC) is a well-known mathematical method employed for solving the hyperbolic equations resulting in multidimensional supersonic flows. This kind of equations have the peculiarity of depending only on a set of initial conditions. The speed of propagation of the perturbations in supersonic regimes is faster than the speed of sound. Therefore, the flow configuration in the divergence part of the nozzle (where the flow is supersonic) only depends on the upstream conditions (the throat conditions). This fact makes possible to use the method of characteristics to solve the flow in the supersonic part of the nozzle. This method has demonstrated to be

useful for the design of nozzle shapes capable of shockwave neutralization but there are more recent methods that have obtained better results. In the present work, we employed the method proposed by Volkov and Galkin for the design of a supersonic nozzle with a corner point and a plane sonic line at the inlet of the supersonic section, and a uniform flow at the exit [41,42]. In this problem it is assumed that the gas is ideal, and the flow is steady, considering an isoenergetic and isentropic flow, these assumptions yield a well-known mathematical formulation of the problem so the flow parameters can be computed using the method of characteristics. Volkov and Galkin proposed an algorithm for the optimization of the nozzle profile which essentially consists in searching for a minimum of a function of several variables at the exit characteristic line of the nozzle [41]. In this method the nozzle profile is described by a cubic B-spline, $f(x)$, with N linearly independent coefficients ($c_1, \ldots, c_N$). These coefficients are calculated to minimize the function $J(c_1, \ldots, c_N)$:

$$J = \left\{ \frac{1}{L} \int_{C_i^+} \left[\left(\frac{\alpha - \alpha_E}{\alpha_I} \right)^2 + \theta^2 \right] dl \right\}^{1/2} + \int_{x_I}^{x_E} \varphi_0(x) dx, \text{ where } \varphi_0(x) = \begin{cases} |f(x)|, f'(x) < 0, \\ 0, f'(x) \geq 0. \end{cases} \quad (3)$$

Where, x is the longitudinal distance along the nozzle axis measured from the plane sonic line, y is the transverse coordinate of the nozzle profile, $y = f(x)$, C_i^+ is the C^+ characteristic line starting at the axis of symmetry towards the nozzle profile, computed at the i-interval along the nozzle axis, which is divided into K intervals from x_I (inlet of the supersonic section) to x_E (nozzle exit section); dl is an element of C_i^+ and $L = \int_{C_i^+} dl$; θ is the angle of velocity vector with x axis; $\alpha = \arcsin(1/M)$ is the Mach angle, with M the local Mach number; $\alpha_E = \arcsin(1/M_E)$ is the Mach angle at the exit section, and $\alpha_I = \arcsin(1/M_I)$ is the Mach angle at the inlet section. Coordinates x_E and y_E are given for a MLN and the Mach at the exit section, M_E is obtained from Eq. (2) of the 1D steady isentropic flow. Then, the function J is minimized when its first term is evaluated along the exit characteristic line by adjusting the ($c_1, \ldots, c_N$) coefficients of the nozzle contour using the Broyden's quasi-Newton method. A nozzle profile was obtained with $N = 10$ and $K = 26$ (see table S1 in the supplementary material for details of optimized nozzle contour).

3. Numerical simulation and experimental verification

In this section we explain the details of the mathematical formulation of the problem for numerical simulation, and the three solvers compared to simulate the supersonic jet features obtained with the basic nozzle. The comparison of the algorithms was carried out by validating their ability to accurately reproduce the shock wave pattern and the evolution of the jet that is observed experimentally in the flow analysis tests using the digital holography technique. This allows to test three solvers and choose the one that most closely represents the flow conditions in our application, in order to use further simulations to refine the design of the optimized nozzle.

3.1. Governing equations

The equations Navier-Stokes equations describe a compressible flow along a supersonic nozzle. Since in reality most flows involve turbulence and in supersonic flows it is especially important, turbulence modeling also had to be considered. In order to reduce the number of the terms in the equations shown below describing compressible flows, the derivatives are going to consider a density-weighted averaging, also known as Favre averaging:

Conservation of the mass:

$$\frac{\partial \bar{\rho}}{\partial t} + \frac{\partial (\bar{\rho} \widetilde{u}_i)}{\partial x_i} = 0 \quad (4)$$

Conservation of the momentum:

$$\frac{\partial (\bar{\rho} \widetilde{u}_i)}{\partial t} + \frac{\partial (\bar{\rho} \widetilde{u}_i \widetilde{u}_j)}{\partial x_j} = -\frac{\partial (\bar{p} + 2\bar{\rho}k/3)}{\partial x_i} + \frac{\partial}{\partial x_j} \left[\mu_{eff} \left(\frac{\partial \widetilde{u}_i}{\partial x_j} + \frac{\partial \widetilde{u}_j}{\partial x_i} - \frac{2}{3} \delta_{ij} \frac{\partial \widetilde{u}_k}{\partial x_k} \right) \right] \quad (5)$$

Conservation of energy:

$$\frac{\partial (\bar{\rho} \widetilde{e})}{\partial t} + \frac{\partial (\bar{\rho} \widetilde{u}_j \widetilde{e})}{\partial x_j} = -\frac{\partial (\widetilde{u}_j \bar{p})}{\partial x_j} + \frac{\partial}{\partial x_j} \left[-q + \mu_{eff} \left(\frac{\partial \widetilde{u}_i}{\partial x_j} + \frac{\partial \widetilde{u}_j}{\partial x_i} - \frac{2}{3} \delta_{ij} \frac{\partial \widetilde{u}_k}{\partial x_k} \right) \widetilde{u}_i - \frac{2}{3} \bar{\rho} k \delta_{ij} \right] \quad (6)$$

where ρ is the density, x_i is the ith component of the position vector, x_j is the jth component of the position vector, u_i is the i^{th} component of the velocity vector, p is the pressure, δ_{ij} is the Kronecker delta, e is the total energy, q is the heat flux vector, $\mu_{eff} = \mu + \mu_t$ represents the effective dynamic viscosity, where μ is the dynamic viscosity and the $\mu_t = \rho \nu_t$ is the turbulent viscosity that depends on the kinematic viscosity, $\nu_t = C_\mu \kappa^2 / \varepsilon . C_\mu$ is an empirical constant and has a value of 0.09, κ represents the turbulence kinetic energy and ϵ the turbulence dissipation rate. Since the turbulence and the changes of density gains prominence in compressible flows, the equations described above used the Favre averaging approach. Favre averaging usually replaces the classical Reynolds decomposition and it separates the turbulent fluctuation from the mean flow. Favre averaging is given by: $\phi = \widetilde{\phi} + \phi''$, where ϕ can be any dependent variable which will be split into a mean part, $\widetilde{\phi}$, and a fluctuating part, ϕ''. The overbars in the equations e.g., $\bar{\rho}$ denotes the averages used by Reynolds decomposition.

3.2. Solvers and simulation details

Here we describe the three solvers with which we have performed the simulations and that we have compared with each other. The *OpenFOAM*® tool has gained many users in the recent years, especially in academia. Its accessibility and high level of modularity makes the software extremely customizable, extending its possibilities to fields other than computational fluid dynamics (CFD). Otto et al. have shown the potential of this tool for simulating laser processing applications [43, 44]. Darwish et al. [45] recently used the CFD solvers of *OpenFOAM* to simulate supersonic flow through a nozzle designed for laser cutting. The model they proposed was then used to predict the behavior of different nozzle designs [46]. The current state of CFD simulation has demonstrated that the tools available are capable of reproducing with precision the flow regimes attained with supersonic nozzles provided the correct model of compressible flow is employed in accordance with specific experimental conditions.

The simulation environment *OpenFOAM* [47] was employed in order to observe the characteristics of the flow generated by the nozzle. The software offers a wide range of solvers for compressible fluid calculations. An analysis of three different solvers (sonicFoam, rhoCentralFoam and pimpleCentralFoam) was carried out comparing their behavior side by side.

The first two are native within *OpenFOAM 6* and can be used for the same type of problems. SonicFoam is a transient solver used for transonic/supersonic regimes suitable for turbulent flows of compressible fluids. By the time of writing this work, the functionality of sonicFoam solver was merged as a transonic option of the application rhoPimpleFoam. This solver was originally constructed for modeling incompressible fluids problems and then patched making it suitable for the compressible case [48]. It uses the PISO (Pressure-Implicit with Splitting Operators) algorithm to couple pressure and velocity. RhoCentralFoam,

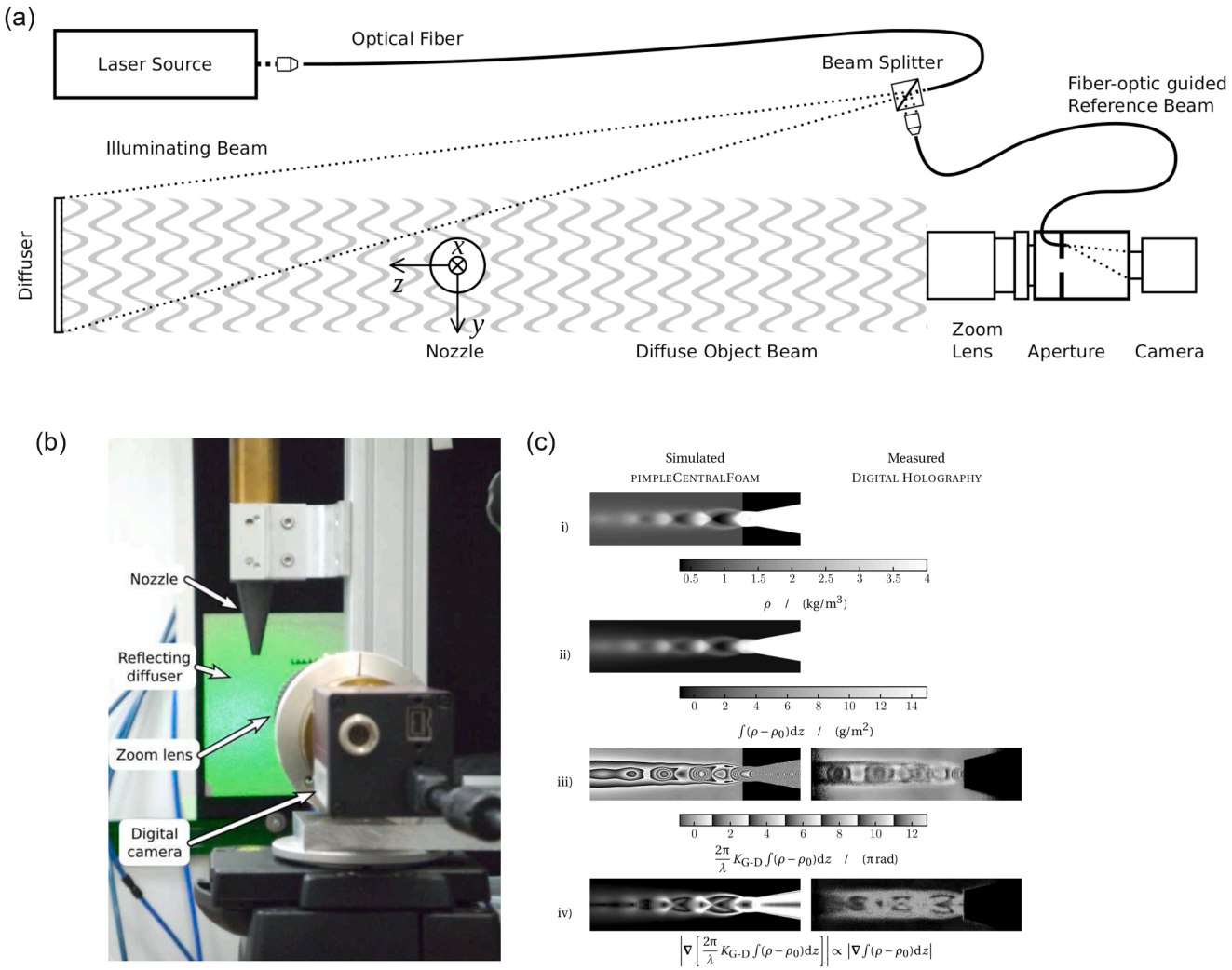

Fig. 3. (a) Schematic representation of the set-up for digital holography. (b) View of the DH system from behind the camera. (c) Procedure to compare the computer simulations (left-hand column) and the actual DH measurements (right-hand column): (i) simulated mass density distribution in the section of the axisymmetric gas jet, (ii) Abel projection of the mass density field, (iii) measured and synthetic *wrapped* phase-change maps, (iv) magnitude of the gradient of the phase.

on the other hand, uses the central upwind schemes proposed by Kurganov et al. (KT/KNP) [49] and implemented for *OpenFOAM* by Greenshields et al. [50]. This method implements an interpolation of the fluxes between neighboring cells that allows for a good modeling of discontinuous solutions such as shock waves [51]. This solver has been proven to achieve the best results out of the two for transonic and supersonic flows, showing the best approximation to the analytical solutions and with more stability than sonicFoam. However, rhoCentralFoam is not able to model subsonic regimes successfully. The KT/KNP schemes have demonstrated good accuracy in solving flows in the sonic/supersonic regime but they fail to work modeling viscous flows at low Mach numbers ($M < 0.3$) [52]. Alternatively, new hybrid schemes have been developed that combine the PISO algorithm, for modeling the case of subsonic flow, with the KT/KNP scheme for solving accurately the discontinuities that appear in supersonic regimes [52]. Moreover, these solvers have been recently improved by allowing the possibility of including outer iterations of the SIMPLE (Semi-Implicit Method for Pressure Linked Equations) algorithm for more accurate solutions [53]. The united collection of all these hybrid solvers is not natively integrated in *OpenFOAM 6* but it can be found in the public repository of the authors. This collection includes a complete set of solvers for a variety of applications, but this work will only review the solver PimpleCentralFoam. It is used for implicit calculation of the main compressible flows equations and the scope of application covers all flow regimes (subsonic, transonic and supersonic). The greatest benefit of using this solver is, that it combines the ability to solve problems with low Mach-number and its accuracy for the discontinuities produced especially at high Mach-number. PimpleCentralFoam runs also stable using second order discretization schemes and delivers, as well, high resolution results for compressible flows [54].

The thermophysical properties of the model and the boundary conditions are the same in all the solvers, but the turbulence parameters are not. On one side, sonicFoam simulations used a κEpsilon (κ-ϵ model) turbulence model. The initial conditions for this set-up were given by:

$$\kappa = \frac{3}{2}(\mathrm{UI})^2 \tag{7}$$

$$\varepsilon = \left(\frac{C_\mu^{3/4}\,\kappa^{3/2}}{L_t}\right) \tag{8}$$

where κ is the kinetic turbulent energy and ε is the turbulence dissipation. κ and $\varepsilon$are derived from the Navier-Stokes equations. The initial values were computed assuming an inlet mean flow velocity $U = 10\ \mathrm{ms}^{-1}$, I is the turbulence intensity and has a value of 0.05 and the turbulent length scale, L_t, is set to a 7% of the inlet diameter. On the other side, pimpleCentralFoam cases were simulated using a κ -Omega model (κ-ω model) and in order to estimates it's initial value the

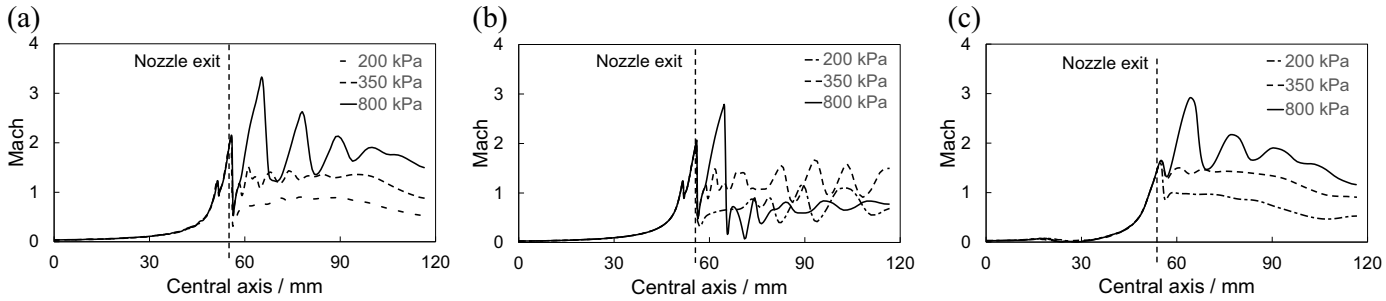

Fig. 4. Simulation results of the Mach number distribution along the central axis of the basic nozzle and the free domain using the three different solvers and three different inlet pressures (absolute pressures) for comparison: (a) results using the pimpleCentralFoam solver, (b) with rhoCentralFoam, and (c) using the sonicFoam solver. The part at the left of the nozzle exit is inside the nozzle and the part at the right is the free jet. The graphs show more realistic results in the simulations performed using the pimpleCentralFoam solver.

following formula was used:

$$\omega = \frac{C_{\mu}^{-1/4}\kappa^{1/2}}{L_t} \tag{9}$$

where ω is the specific dissipation rate. RhoCentralFoam does not include turbulence modeling. The model was weakly dependent on the turbulence parameter value, hence the same values were used independently of the stagnation pressure.

3.3. Flow visualization and comparison with simulations

In order to perform the experiments of flow visualization, we installed the nozzles in an optical metrology laboratory under controlled ambient conditions. They were mounted in vertical position with the filament and air-jet flowing downwards to avoid any distortion by gravitational forces. The nozzle was feed with compressed air through a circuit with sufficient capacity to ensure the mass flow rate necessary to produce choking at the throat (sonic regime) for all the pressures used. Moreover, we installed a reservoir tank close to the nozzle with a double aim: to accurate measure the stagnation pressure of the air supplied and to guarantee the mass flow required by the supersonic nozzle. To carry out the experiments to visualize the oscillation of the filament, we placed a pure silica fiber with a 600 μm diameter in the central guide conduct that passes through the center of the nozzles.

The actual distribution of mass density in the air jet has been measured by digital holographic interferometry [55]. This kind of measurement has been demonstrated in the past by using, among others, Mach-Zehnder [56], multiple wavelength [57] and even multidirectional [58] digital holographic set-ups. In this work, a *quasi*-Fourier transform digital holography system [59], arranged for the measurement of phase objects in a single-pass configuration (Fig. 3a), was used. The beam of a continuous-wave Nd:YAG laser, with wavelength $\lambda = 532$ nm, is launched into a polarization-maintaining monomode optical fiber and split in an object and a reference beam. The object beam diverges from the fiber end and illuminates a reflecting diffuser (an anodized aluminum plate) placed behind the nozzle (Fig. 3b). The scattered beam passes through the gas jet and a photographic objective forms an image of the plane of the jet on the plane of a field-limiting aperture.

The reference beam is guided through a second optical fiber to the plane of the aperture. Both beams propagate together from the plane of the aperture to a plane conveniently apart (see Ref. [59]) to interfere and form a *quasi*-Fourier transform hologram that is recorded with a digital camera. The sensor of the camera has 2448 × 2050 pixels, each of them with an area of 3.45 μm × 3.45 μm. The exposure time of the hologram is controlled with the electronic shutter of the camera.

To measure the mass density distribution in the gas jet, a reference hologram is recorded with the air at rest and a second hologram is taken with the jet flowing out of the nozzle. Both holograms are numerically reconstructed by means of Fourier transforms and the resulting values of the optical phase are subtracted. The change of the optical phase $\Delta\phi$ is related to the projection of the changes of refraction index of the air induced by the jet along the observation direction z [60] which, in turn, are proportional to the changes in the density of the air [34]. Consequently, it can be written as

$$\Delta\phi = \frac{2\pi}{\lambda} K_{G-D} \int (\rho - \rho_0) dz \tag{10}$$

where $\rho = \rho(x,y,z)$ is the mass density field inside the gas jet, ρ_0 is the mass density of the surrounding air, and $K_{G\text{-}D}$ is the Gladstone-Dale constant. The optical phase is calculated with an arc tangent function and, therefore, the resulting phase-change maps are "wrapped" into the interval $(-\pi,\pi]$ (Fig. 3c–iii, right hand image).

Since the gas jet is assumed axisymmetric, the projection in Eq. (10) is an Abel transform. Applying an Abel inversion after unwrapping the measured phase-change map should yield an estimation of the local mass density distribution in the section of the actual gas jet which may be compared to the results of the numerical simulations [61]. But both steps in that approach, phase unwrapping and Abel inversion, have a tendency to accumulate the measurement errors and the later is highly sensitive to the misalignment of the axis of symmetry. To circumvent these drawbacks, the opposite procedure has been taken instead: Eq. (10) is applied to the simulated mass density fields, by using a numerical Abel transform [60], to get synthetic wrapped phase-change maps (Fig. 3c–iii left hand image) that are compared with the measurements (right hand image). The value of the Gladstone-Dale constant for the wavelength of the laser and the temperature, humidity and pressure of the atmospheric air that is compressed to feed the nozzle, has been obtained by dividing the value of the refractivity calculated with Ciddor's equation [62] by the value of the mass density calculated with the CIPM-2007 formula [63].

A visually effective representation of both the measurements and the simulations, that is similar to the images yielded by the well-known *Schlieren* technique, is generated by computing the magnitude of the gradient of the corresponding phase-change maps [64]. In this case the calculation of the gradient has been implemented by using the Prewitt discrete differentiation operator, the obtained images are identified as Gradient of Optical Phase (GOP) maps (Fig. 3c–iv).

A further operating mode has been implemented to visualize the instabilities in the mass density distribution of the gas jet, as well as the oscillation of the glass filament. This mode consists in the acquisition of a single time-averaged digital hologram with a relatively long exposure time (in the order of tens of milliseconds). The magnitude of the numerical reconstruction of such holograms shows dark/bright fringes in the regions where the mass density distribution changes during the exposure time, thus revealing the instabilities of the gas jet in the images labeled Time-Averaged Holographic Reconstruction TAHR) maps (see right hand block of Fig. 8 in Section 4.3). The frequency of the flow

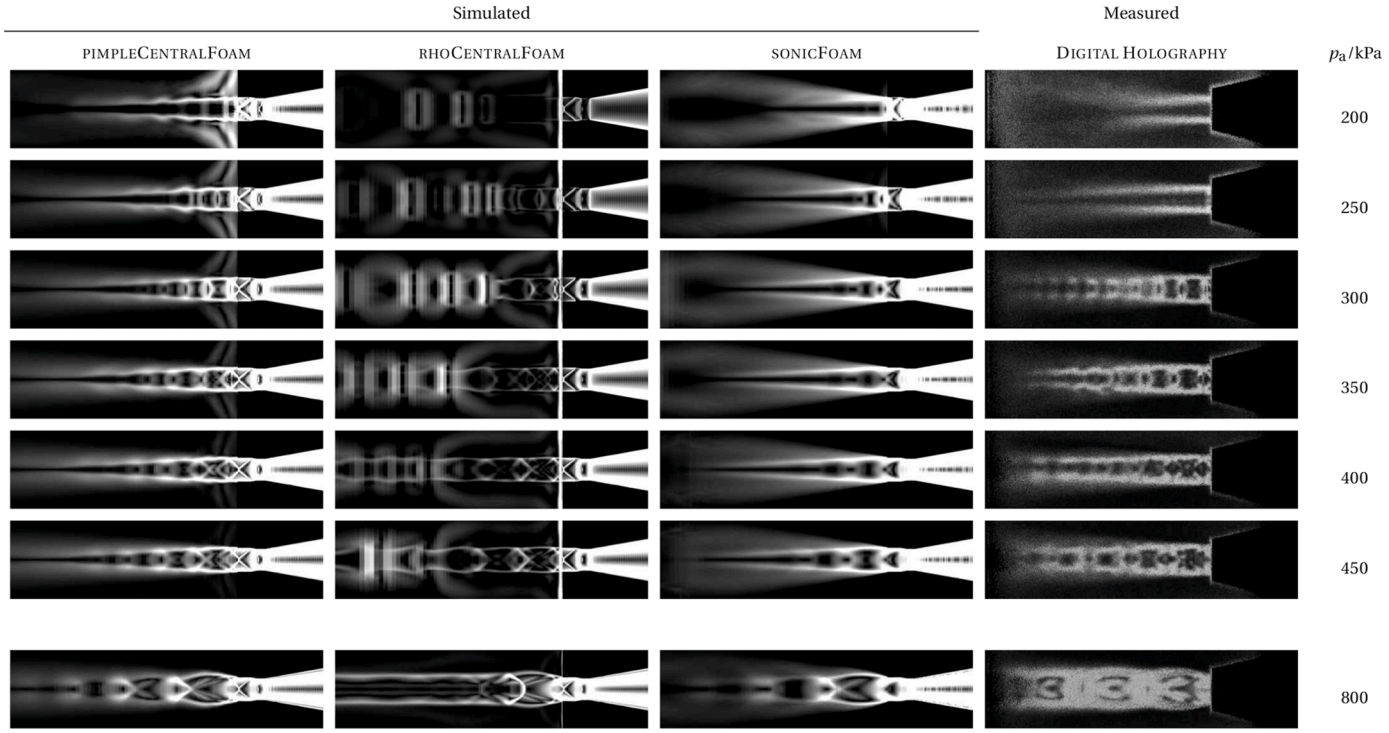

Fig. 5. Comparison of the three solvers and the GOP map experimentally measured by digital holography for different absolute stagnation pressures as indicated for each row (p_a states for absolute stagnation pressure). The images show the magnitude of the gradient of the simulated and measured phase-change, respectively, revealing the mass density gradients, which are especially intense in the pressure jumps produced by shock waves. The contrast of each image is individually equalized to highlight the features of the gradient distribution rather than to compare the magnitude between images. The comparison of the shock wave pattern obtained using the three solvers with the GOP map measured by DH shows that the results obtained with the pimpleCentralFoam solver present greater fidelity with the experimental measurements.

unsteadiness and filament oscillation captured with this technique is in the order of hundreds of hertz or higher, since the minimum exposure time used was 5 ms. This operating mode is more adequate to observe the filament oscillation because in this case its motion is not masked by the spatial distribution of the gradient of the mass density distribution in the flow produced by the shock wave pattern, which is distinctively captured in the gradient of optical phase maps.

4. Results and discussion

In this section we first present the comparison of the flow simulations using the three solvers and validate them against the results of optical measurements, which lead us to select the algorithm that more closely simulate the flow in all regimes. A quick analysis of the design faults of the frustoconical nozzle will be related with the oscillation of the filament in the last section. The simulations using the selected solver will support the choice of the optimum design of the nozzle, which is tested in a new set of flow visualization experiments. Finally, in the last section we perform an experimental analysis of the oscillation of the filament at several operating pressures using two different techniques of flow measurement. Furthermore, comparing the performance of the frustoconical nozzle with the optimized nozzle facilitates the analysis of the causes of the filament oscillation.

4.1. Comparison of solvers

The frustoconical nozzle was tested with the three solvers under three different stagnation pressures (absolute pressures): 200 kPa (over-expanded jet), 350 kPa (optimally expanded jet) and 800 kPa (under-expanded jet). Fig. 4 shows the results of the Mach number in the domain of the simulations.

The Mach number contours show that, overall, the three solvers model the flow in a similar manner, specially inside the nozzle and in points of the jet close to the nozzle exit. However, there are clear disparities that must be noted. Whereas pimpleCentralFoam and sonicFoam appear to present a similar configuration of the exit jet, rhoCentralFoam presents a different pattern of Mach oscillation which is directly related with the formation of shockwaves in the jet. The patterns obtained with the solver rhoCentralFoam for the stagnation pressures of 200 and 350 kPa show an unusual amplification of instabilities along the free jet instead of the expected dissipation of the shockwaves. This anomalous flow behavior is confirmed with the comparison of the jet simulations using the three solvers in comparison with the experiments of optical measurements presented in Fig. 5. The comparison of the shock wave patterns simulated using the three solvers reveal that sonicFoam and pimpleCentralFoam model the flow behavior in a more realistic way, while rhoCentralFoam produces an inconsistent amplification of the shock wave strength as the jet flows away the nozzle exit. Moreover, in the results for a stagnation pressure of 800 kPa, rhoCentralFoam presents a Mach disk resulting from the violent expansion of the jet. This feature is not present in the flow modeled by the two other solvers nor in the experimental results. Downstream the point of formation of the Mach disk the flow appears uniform and the Mach number along the axis line is considerably reduced reaching the subsonic regime. Additionally, PimpleCentralFoam appears to model more precisely the abrupt pressure changes resulting in a sharper definition of the shockwaves. RhoCentralFoam shows a similar behavior but fails to model correctly the dissipation of the downstream part of the jet. SonicFoam shows a smoother transition of density throughout the domain modeling the shockwaves less sharply. Overall, the average values of Mach number and the phase gradient maps in the downstream part of the jet are the same as obtained with pimpleCentralFoam, but the results obtained with sonicFoam seem a blurred version of the ones obtained with pimpleCentralFoam. However, some instabilities can be noticed in the

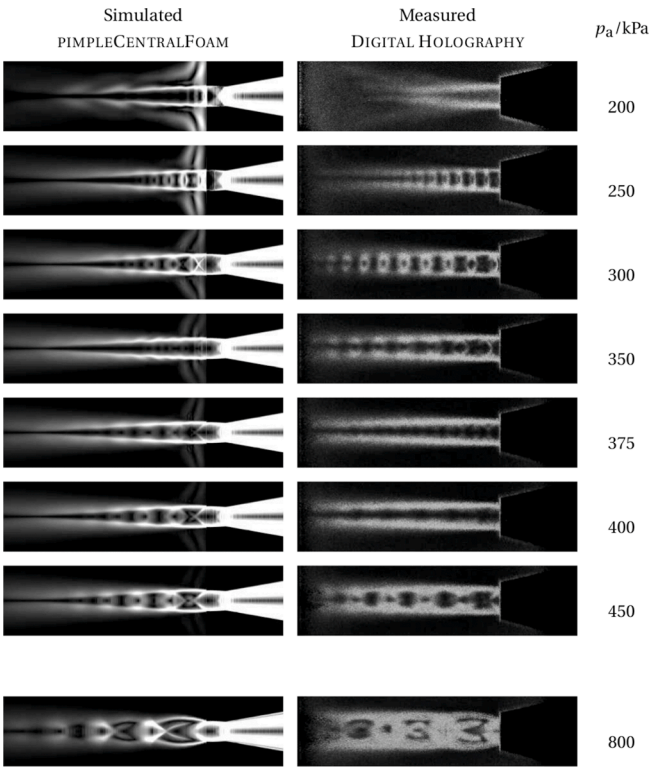

Fig. 6. Phase-gradient maps of the mass density distribution in the free jet generated by the optimized nozzle supplied with compressed air at different stagnation pressures (p_a states for absolute stagnation pressure). The simulated GOP maps are obtained by processing the mass density fields calculated using the pimpleCentralFoam solver. The measured images are the GOP maps obtained in the DH experiments. The simulation shows an optimum working point at an absolute pressure of 350 kPa, while the measured GOP map reveals a perfectly expanded and free of shock waves jet at the pressure of 400 kPa. The reason for this difference may be due to small variations in the construction of the nozzle with respect to the design or to an underestimation of the friction losses in the calculations.

middle section of the convergent part of the nozzle in the sonicFoam simulations.

In sum, the simulations performed with rhoCentralFoam did not resolve accurately the jet supersonic features, the flow presents anomalous instabilities in the jet and shows a Mach shock disk that is not observed in the DH measured air flow with 800 kPa of stagnation pressure. The simulations with SonicFoam match the shockwave pattern at 800 kPa but is unable to clearly show the oblique shockwaves that appear at 350 and 400 kPa. It shows a much smoother jet compared to the experimental results. The simulations that more closely reproduce the free jet pattern are done with pimpleCentralFoam. These results show with notable precision the position of the shockwaves at any given pressure as well as the diamond structure of oblique compression and expansion waves observed at 400 kPa in the maps of phase gradient measured with DH. The intensity of the shockwaves at 800 kPa seems slightly weaker than those observed in the experimental results, but the simulation shows a clear depiction of the shockwave pattern in the free jet. On the other hand, the further propagation of these expansion and oblique shock waves through the free jet provokes the fluctuation of the flow velocity which can also be appreciated in the Mach number graph (Fig. 4a). It is concluded that pimpleCentralFoam is the optimum choice among the solvers tested, based on our experimental analysis, and that it can model with accuracy the flow behavior at these regimes. For this reason, we selected this algorithm to support the next stage of optimized nozzle design.

4.2. Optimization of the nozzle

The results presented in the previous section for the basic frustoconical nozzle reveals several outcomes of its defective design: the formation of oblique shock waves in the divergent section and a Mach shock disk at the exit of the nozzle, which can be attributed mainly to the simplified conical profile of the nozzle and the excessive angle of divergence. For this reason, we tackle the task of designing and manufacturing an optimized nozzle. The simulations performed with the solver pimpleCentralFoam reveal a weak Mach shock disk formed at the exit of the frustoconical nozzle. It can be noticed in the GOP maps of mass density for the stagnation pressures from 250 kPa up to 350 kPa (see Fig. 5). This Mach disk appears at the exit point of the oblique shock waves generated in the divergent section. Furthermore, the simulations bring to light well defined shock waves developed at the beginning of this divergent section, which effect is also unveiled in the Mach number graphs presented in Fig. 4a, represented as a sudden drop of the flow velocity at 50 mm from the starting point of the simulation independently of the operating pressure. This may be explained by the defective design of the nozzle: the flow deflection angle induced by the frustoconical surface used in the divergent section of the basic design nozzle exceeds the Prandlt-Meyer angle for the Mach number estimated according to the 1D model [65]. In fact, the Prandtl-Meyer angle for exit Mach of 1.46 is 10.73°, which is effectively inferior to the divergent angle in the basic nozzle (19.4°). As a consequence, the internal flow suffers of boundary layer detachment and the jet develops the typical pattern of successive expansion and oblique shock waves even at the stagnation pressure for which the nozzle was designed, i.e., 350 kPa, which is also transmitted to the free jet, as can be clearly appreciated in the simulations and in the experiments measured by digital holography. In fact, according to the optical analysis of the free jet, the optimum conditions to operate this nozzle in order to generate a clear air flow field, without supersonic instabilities, is the lowest pressure of 200 kPa, which on the contrary does not produce a supersonic flow but a subsonic one. In the next section we will analyze the detrimental effect of the former separated flow induced instabilities on the oscillation of the filament, which lead to strong whipping. Here, we are presenting the design of an optimized nozzle developed with the aim of reducing these deficiencies and to make possible the analysis of their effect by comparison.

We tested various methods to generate simple and easy-to-manufacture profiles for the design of the optimized nozzle, such as reducing the divergence angle. We also compared the profiles calculated by the method of characteristics using the gradual expansion nozzle and Minimum Length Nozzle (MLN) criteria. The comparison of the simulations carried out with these profiles finally led us to adopt the MLN profile obtained using the Galkin algorithm already mentioned [41], since this profile yielded a perfectly expanded air jet without perceptible shockwaves in the simulations. Consequently, an optimized nozzle with the same throat diameter and design Mach number of 1.46, equivalent to the basic nozzle, was manufactured by electrical discharge machining to obtain a precise and smooth profile (details of the nozzle profile are presented in the supplementary materials section). This nozzle was tested with the aim of experimentally compare its performance with the basic frustoconical design.

Fig. 6 presents a comparison of the CFD simulations and experimental optical measurements by DH of the free jet generated for different supplied stagnation pressures using the optimized nozzle manufactured with the MLN profile obtained from the Galkin's MOC algorithm. Both the simulations and the experimental measurements reveal a working point for which the internal flow and the free jet are completely free of perceptible shock waves, although the working point differs slightly between them. In the case of the simulated free jet, the optimum working pressure exactly coincides with the design pressure of 350 kPa, however, the experimental observations showed that this value must be displaced to a somewhat higher pressure of 400 kPa. The cause

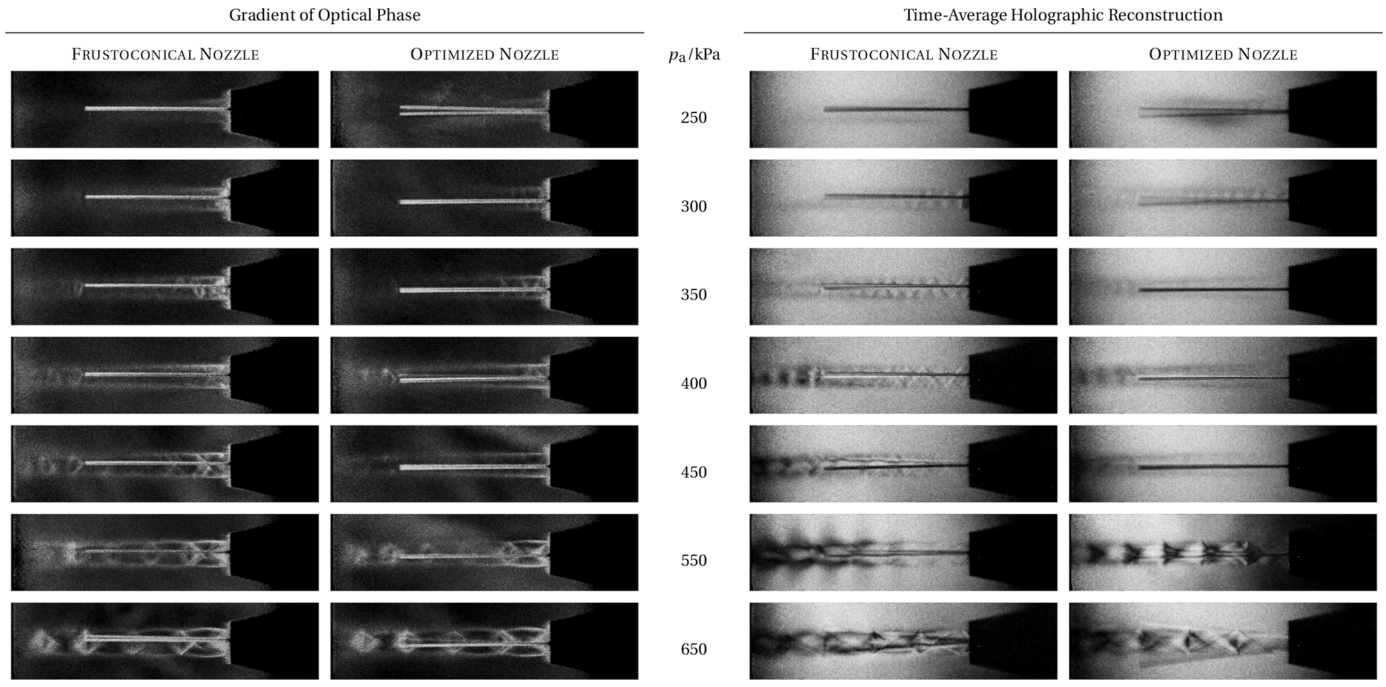

Fig. 7. Comparison of the optical measurements of the air jet with the glass filament using both nozzles for different stagnation pressures. The GOP map reveals the spatial variation of the flow pressure, whereas the TAHR map is sensitive to temporal variations of pressure. The oscillation of the filament can be noticed in the time-average holographic reconstructions. Both the GOP and the TAHR images have been individually equalized to optimize the visibility of the features in the gas jet. This analysis demonstrates the existence of an optimum working point using the optimized nozzle at pressure of 450 kPa. Furthermore, it also reveals how the filament oscillation can be induced both by the appearance of shock waves in the GOP map or regions of temporal unsteadiness of pressure in the TAHR images.

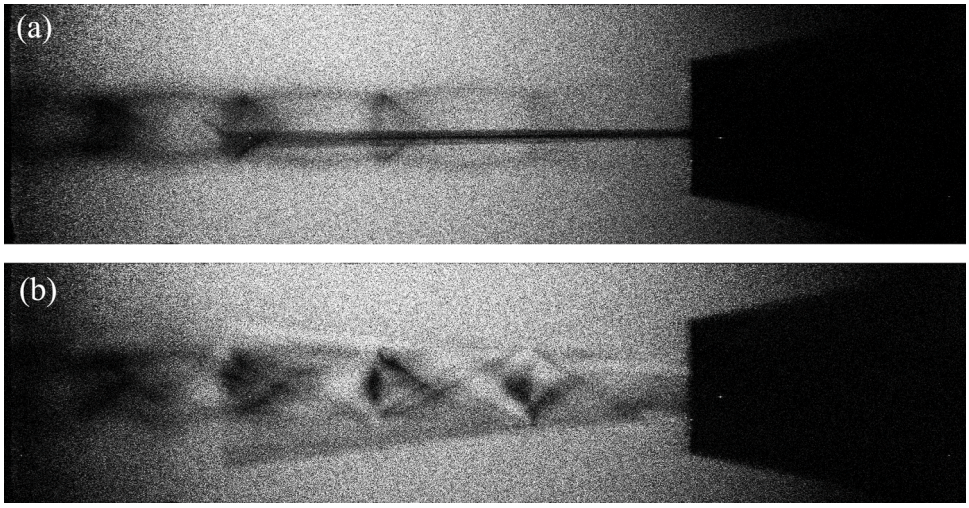

Fig. 8. TAHR maps of the jet generated by the optimized nozzle operating at pressure of 650 kPa in two separate snapshots that are differentiated by the oscillation of the filament: (a) stable filament, (b) oscillating filament. The comparison reveals how the oscillation of the filament has a noticeable effect on the temporal variation of the pressure.

for this disparity between simulation and experimental measurements may arise for two different reasons: one may be a slight deviation of the manufactured profile from the designed one, and the second may be an underestimation in the simulations of the friction losses of the flow along the solid boundaries of the nozzle and the conducts. In any case, these results are very useful to verify the efficacy of the optimized nozzle to generate a jet without shock waves and to emphasize the need to analyze the design experimentally in order to correctly determine the optimum working point. Notwithstanding, this optimum working point might eventually be corrected by the presence of the filament in the air flow.

4.3. Analysis of filament oscillation

In order to analyze the influence of the supersonic features of the air jet on the oscillation of the filament, we present a comparison of the performance of the supersonic flow generated by the basic frustoconical nozzle and the nozzle with the optimized profile; notice that both nozzles are designed for the same exit Mach number and throat diameter. Fig. 7 presents the comparison of the optical measurements of the air jet and filament oscillations using both nozzles for different stagnation pressures. Two different complementary techniques of flow visualization are presented: the gradient of the optical phase and the time-

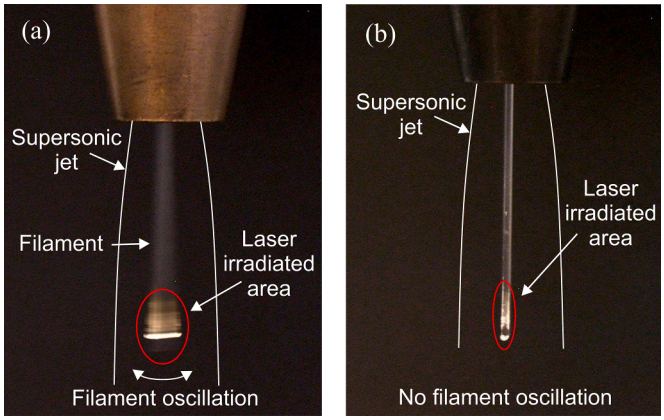

Fig. 9. Graphical comparison of the wide cross-sectional area of the laser beam needed under the conditions of high filament oscillation produced by the basic nozzle design for Cofiblas (a) and the reduced area when oscillation is reduced using the optimized nozzle (b). Note that these optical images do not allow showing the gas jet, therefore it is delimited by white lines in the images. The reduction of the filament oscillation when using the optimized nozzle allows to significantly reduce the cross-sectional area of the laser beam, which implies a significant increase in the efficiency of the process.

average holographic reconstruction. The first technique reveals the instantaneous pattern of the mass density (fluid pressure) spatial variation and demonstrates a high sensibility to detect the presence of shockwaves, as we could see in the previous experiments. Conversely, the TAHR is specifically appropriate to detect the oscillation of the filament and, also, to visualize the temporal instabilities of the mass density at specific regions during the exposure time. That is, this technique allows detecting the regions where temporal variations of the fluid pressure occur, specifically, with the exposure times employed it is sensitive to unsteadiness in the flow with frequencies of hundreds of hertz or higher. The combination of both techniques allows to compare the effect of the shockwaves and flow unsteadiness on the appearance of the filament whipping.

The first observation is that the optimized nozzle can be operated at high pressures between 350 and 450 kPa without inducing a perceptible filament oscillation, as can be appreciated in the time-averaged images. Conversely, the frustoconical nozzle provokes filament whipping at all pressures higher than 250 kPa, and these oscillations increase gradually with increasing pressure.

These results demonstrate that the filament oscillation can be directly related with the presence of shockwaves and pressure unsteadiness in the jet. In fact, the presence of a significant mass density spatial variation, characteristic of shock waves detected in the GOP maps of the optimized nozzle for pressures of 550 kPa and higher, provokes a filament oscillation clearly visible in the time-averaged images. The presence of shock waves produces a deflection of the air flow that induces radial components of the velocity, which cause the oscillation of the filament. This is consistent with previous aerodynamical analysis of the melt-blowing process which demonstrated that a small lateral component of the velocity has a crucial effect on initiating oscillation of the filament or whipping [26]. Conversely, when it is operated at the pressure of 450 kPa a perfectly expanded jet is observed, no spatial (GOP map) or temporal (TAHR map) variation of pressure is perceived, which translates into a perfectly static filament free of any oscillation. Similarly, when the optimized nozzle is operated at the pressures of 350 and 400 kPa, only weak variations can be detected in the GOP map of the jet, however they do not seem to have a sufficient intensity to produce the oscillation of the fiber. Perhaps this is because the glass fiber has a sufficiently high stiffness that requires a minimum threshold of the instabilities to cause its oscillation.

A second effect may be related with the appearance of regions of temporal unsteadiness in the mass density of the jet, which can be distinguished in the time-averaged images as alternating dark and bright fringes. This temporal instability can induce a filament oscillation clearly perceptible in the TAHR images even when the intensity of the shock waves is almost imperceptible in the GOP maps. This phenomena in the absence of perceptible shock waves can be clearly noticed in the frustoconical nozzle operated at pressure of 400 kPa (design pressure) and the optimized nozzle at pressures below 350 kPa. Interestingly, although it is not possible to detect any shock wave in the jet generated by the optimized nozzle operating at pressures of 250 and 300 kPa, the oscillation of the filament is clearly perceptible. Below the design pressure, the characteristic unsteadiness of an overexpanded flow was recently demonstrated to induce flow separation and low frequency pressure fluctuations into the nozzle that are transmitted downstream to the external flow as high frequency velocity fluctuations [66], generating fluctuating side loads which may be responsible of the filament oscillation. Analogously, in the frustoconical nozzle at the design pressure, a similar kind of pressure fluctuations may be provoked by the defective design of the divergent section with an angle higher than the Prandlt-Meyer angle, leading to the appearance of shock waves in the internal flow which induce flow separation and the external pressure fluctuations responsible of filament oscillation.

The combined analysis of the effect of the shock waves and temporal fluctuation of pressure reveals their strong interaction. As we already stated, the appearance and progressive intensification of the shock waves in the GOP maps for both nozzles, due to the gradual increase of pressure over 450 kPa, produce an increasing agitation of the filament, while, at the same time, the presence of the filament induces a stronger instability, which can be noticed in the TAHR images. The oscillation of the filament may also be related with the low frequency unsteadiness of the lateral pressure characteristic at the zone of interaction of the shock wave with the boundary layer, which was well characterized experimentally for a supersonic flow over a compression ramp [67]. Whereas a later critical review concluded that the characteristic motion upstream and downstream of this separation shock is also strongly similar across all separated interactive flows [68], therefore it is reasonable to think that the behavior is also similar in the present case. Additionally, a recent analysis of the causality of the unsteadiness of the shock wave boundary layer interaction demonstrates that the downstream fluctuations propagate upstream and lead to shock wave oscillations [69] which may explain the presence of the strong temporal fluctuations on the pressure map captured in the TAHR images at pressures of 550 and 650 kPa for both nozzles. In these cases, the downstream fluctuations in the flow may be intensified by the filament oscillation promoted by the high intensity of the shock waves, then propagating upstream and increasing the temporal unsteadiness of pressure due to the spatial oscillations of the shock waves. This self-energizing effect can be observed when comparing the TAHR images of the flow with and without filament oscillation. Fig. 8 presents a comparison of the TAHR maps obtained for the optimized nozzle operating at same pressure of 650 kPa in consecutive tests and with exactly the same optical measurement conditions (exposition time and illumination), whereas in the first image the filament is static and in the second one is oscillating. This comparison can be performed because the oscillation of the filament is not continuous but intermittent. The difference in the oscillation of the filament is clearly transmitted to the stability of the pressure map, the temporal variation of pressure is notably increased when the filament is oscillating. Consequently, we show here that, the presence of the filament increases the spatial instability of the shock wave pattern and, subsequently, a self-energizing increase of the pressure unsteadiness. This experimental evidence of the turbulence energizing effect of the filament oscillation is in good agreement with the already reported numerical simulations of the flexible flat panel fluttering induced by shock wave boundary layer interaction, which clearly results in an increased level of flow turbulence downstream [70,71].

Finally, the optimization of the air flow has an important effect on

the Cofiblas and melt-blowing processes. First it produces the maximum drag force on the filament in steady regime, thanks to the absence of shock waves and turbulences. Consequently, it yields the highest stretching stress in the filament which may be able to elongate it down to the nanometric regime in stable regime. This allowed the unprecedent continuous production of glass nanofibers as demonstrated in a previous work [35]. Additionally, the reduction of the filament oscillation allows a more precise adjustment of the cross-section of the laser beam in the Cofiblas process, since the oscillation forces to cover a very wide area around the filament with the laser radiation to guarantee that the filament is continuous and homogeneously irradiated at any time (see Fig. 9). Then, the stationary position of the filament allows to reduce the cross section of the laser beam in the direction transversal to the filament, and, it has a very significant and positive effect in controlling the irradiance pattern of the laser beam on the molten filament, which was recently demonstrated to have a crucial influence in achieving adequate heating of the filament for nanofiber production [72]. Both improvements together involve a significant reduction of the radiant power compared to the large cross-sectional area of the beam necessary to heat the oscillating filament. Consequently, the optimization of the supersonic nozzle entails a worthy increase of the process efficiency as the laser power required to heat the filament is reduced by an order of magnitude. These results have become patent from the first experimental tests of Cofiblas carried out with the optimized nozzle.

5. Conclusion

In order to produce polymer or glass nanofibers the melt blowing and the Cofiblas processes require careful design of a supersonic nozzle to minimize the formation of shock waves and turbulences in the air jet, since these instabilities induce the oscillation and sometimes strong whipping of the filament compromising the stability of the process. With this premise, we employed a combination of CFD simulations and experimental techniques of flow visualization to analyze the performance of a basic nozzle, having a simplified frustoconical profile, and to compare it with an optimized nozzle with a profile calculated considering the multidimensional characteristics of the flow.

The comparative analysis using two methods of flow visualization allows to capture the influence of the shock waves and flow unsteadiness on the oscillation of the filament. On one hand, the maps showing the gradient of optical phase are highly sensitive to spatial variations of flow pressure and, consequently, to the presence of shock waves in the free jet. In this way, the oscillation of the filament becomes more violent as the intensity of these shock waves increases. Conversely, the time average holographic reconstruction is responsive to temporal changes of flow pressure in the same point, therefore it allows to detect flow unsteadiness. By means of the TAHR we detected the flow unsteadiness in the free jet of the optimized nozzle working in overexpanded regime and of the frustoconical nozzle working at the design pressure even when any shock wave can be detected in the GOP maps. This flow unsteadiness provoked by internal shock waves and flow separation also produce perceptible filament oscillation. In addition, a complementary analysis of the GOP maps and the TAHR images allowed us to verify that the combined effect of shock waves and filament oscillation at high pressures provokes a self-energized temporal instability of the flow pressure compared with the stationary condition of the filament.

On the contrary, the optimized design of the nozzle operated at proper pressure avoids the formation of shock waves, reduces the unsteadiness of the flow and avoids the oscillation of the filament. This regime yields a maximum and stable drag on the filament which allows the continuous production of nanofibers. This optimization process can also be applied to the design of nozzles for melt blowing of polymers avoiding the instabilities inherent to the use of high pressures. The use of a suitable supersonic nozzle can increase the elongation effort on the filament to reduce the diameter of the fibers down to the nanometric range.

In future works, the digital holography technique might be employed to analyze the frequency of the filament oscillation and the flow unsteadiness by adjusting the exposure time employed to record the holograms of the jet. Then the frequency of these events might be related to the causes and give more evidences on the origins of these instabilities.

Funding

This work was partially supported by the EU research project Bluehuman (EAPA_151/2016 Interreg Atlantic Area), Government of Spain [PGC2018-094,900-B-I00 (MCIU/AEI/FEDER, UE), FPU20/03,112], and by Xunta de Galicia (ED431C 2019/23).

CRediT authorship contribution statement

F. Quintero: Conceptualization, Visualization, Investigation, Funding acquisition, Writing – review & editing. **A.F. Doval:** Visualization, Conceptualization, Investigation, Writing – review & editing. **A. Goitia:** Conceptualization, Visualization, Investigation. **R. Vázquez:** Conceptualization, Writing – review & editing. **K. Crespo:** Conceptualization, Writing – review & editing. **R. Barciela:** Visualization, Investigation. **M. Fernández-Arias:** Visualization, Investigation. **F. Lusquiños:** Conceptualization, Funding acquisition, Writing – review & editing. **A. Otto:** Conceptualization, Writing – review & editing. **J. Pou:** Conceptualization, Funding acquisition, Writing – review & editing.

Declaration of Competing Interest

The authors declare the following financial interests/personal relationships which may be considered as potential competing interests: Felix Quintero Martinez has patent #EP 3 372 712 B1. METHOD AND DEVICE FOR GENERATING CONTINUOUS FIBRES HAVING A NANOSCALE DIAMETER AND NANOSCALE FIBERS GENERATED issued to Universidade de Vigo.

Data Availability

Data will be made available on request.

Acknowledgments

We acknowledge the help of A. Abalde with the construction of the nozzles and experimental system.

Supplementary materials

Supplementary material associated with this article can be found, in the online version, at doi:10.1016/j.ijmecsci.2022.107826.

Appendix A. Simulation domain and physical properties

Table A.1 summarizes all the parameters used for the reduced proposed nozzle geometry shown in Fig. 2b. The simulation domain takes into account only the part of the nozzle downstream of the last stabilizing section, saving a lot of computational effort. This simplification was tested by comparison with the simulation of the whole geometry obtaining the same results in both cases. The simulation domain is composed by the nozzle geometry and an open-air section to observe the quality of the exit jet. Since the nozzle shape is axisymmetric, the control volume solved in the simulations is a 2.5° wedge, not the full 3D geometry. This simplification reduces greatly the computation time and assumes that the azimuthal component of the flow is negligible.

Table A.2 shows the fluid parameters used for the set-up of the simulation cases.

Table A.1
Nozzle parameters.

Parameters	Value
Inlet diameter (D_I / mm)	22.63
Throat diameter (D_T / mm)	5
Exit diameter (D_E / mm)	5.5
Nozzle length (L_N / mm)	56.42
Convergent length (L_c / mm)	50
Throat length (L_T / mm)	2
Divergent length (L_D / mm)	1.42
Exit channel length (L_E / mm)	3
Buffer length (L_B / mm)	60

Table A.2
Fluid parameters.

Fluid parameters	Value
Dynamic viscosity (μ / kg m^{-1} s^{-1})	1.789×10^{-5}
Kinematic viscosity (ν / m^2 s^{-1})	1.46×10^{-5}
Molecular weight (M_w / g mol^{-1})	28.90
Specific heat ratio (γ)	1.4
Gas constant (R / J mol^{-1} K^{-1})	8.314
Density (ρ / kg m^{-3})	1.225

Appendix B. Mesh generation

For the mesh generation the axisymmetric wedge type was used in order to reduce efforts in the set-up of the geometry and the computational time. Despite the results are displayed in 2 dimensions, Fig. B.1 shows the mesh implemented in an axisymmetric geometry of a nozzle sector that covers a 2.5° wedge, not the full 3D geometry. The geometry used in Darwish et al. [45] paper is the starting point to generate the mesh that is presented in Fig. B.1. The setup of this well-documented work was recreated with the purpose of validating the results and to use this as a guide to set up initial conditions and the geometry parameters. Although this work uses a larger geometry, it was possible to keep roughly the number of cells used in Darwish et al. [45] paper. The current design has 14,250 cells and a maximum skewness of 0.33. The cell size in the throat is about 0.1 mm and it counts with a buffer section with the length of 60 mm and a diameter of 22.63 mm. The geometry owns six blocks. An advantage in this work is that the simulation results had used a post-processing tool and directly compare them with the experimental results. The mesh presented in Fig. B.1 is a zoom into the throat and exit of the nozzle and was used for all simulations with rhoCentral-, sonic- and pimpleCentralFoam. The aim of this evaluation is to show which of the three solvers employed here, was closer to the reality; since the mesh used presented already an enough resolution for simulating shockwaves and award very close solutions compared to the experimental results, reducing cell sizes and the possible differences presented between these refinements was not necessary.

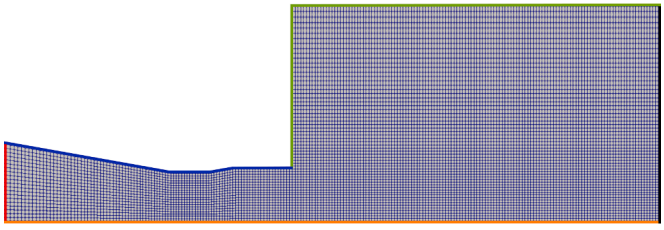

Fig. B.1. Zoom in the throat and exit of the nozzle showing the mesh implemented in an axisymmetric geometry of a nozzle sector that covers a 2.5° wedge.

Table B.1
Simulations control parameters.

Parameters	Value
Time step (δt / ms)	1×10^{-8}
Mesh size (δx / mm)	5×10^{-2}

To generate the geometry and define initial and boundary conditions a configuration was needed. The red part was configurated as the inlet, the blue part as wall, the green part as atmosphere, the black part as outlet and the orange part as axis. Some other parameters, for instance control parameters are also important to be considered and are described in Table B.1.

Appendix C. Initial and boundary conditions

The initial and boundary conditions were for all solvers the same. The differences are in the set-up of the turbulence models, since rhoCentral Foam uses a laminar simulation type, pimpleCentralFoam a kOmega, κ-ω, model approach and sonicFoam is simulated with a κEpsilon κ-ϵ turbulence model.

Tables C.1 and C.2

Table C.2
OpenFOAM boundary conditions clarification.

totalPressure (p_a)	$p_a = p + \frac{1}{2}\rho U^2$
pressureInletOutletVelocity	Inflow: $U = (0, 0, 0)$; Outflow: $\nabla U = 0$ Velocity is adjusted by pressure.
fixedValue	Constant value in the boundary
zeroGradient	$\nabla = 0$
noSlip	U= (0,0,0)
inletOutlet	Inflow: fixedValue; Outfow: zeroGradient
waveTransmissive	Allows for the transmision of shockwaves outwards of the domain
kqR,epsilon, omegaWallFunction	Wall function to model viscous layer

Table C.1
Boundary conditions imposed at each boundary section to the following variables: p, pressure; U, mean flow velocity; T, temperature; κ, turbulence kinetic energy; ϵ, turbulence dissipation; ω, specific turbulence dissipation.

Variable	Inlet	Open-air	Outlet	Walls
p	totalPressure (absolute stagnation pressure p_a)	totalPressure (101,325 Pa)	waveTransmissive (101,325 Pa)	zeroGradient
U	pressureInletOutletVelocity	pressureInletOutletVelocity	inletOutlet	noSlip
T	fixedValue (293 K)	fixedValue (293 K)	inletOutlet	zeroGradient
κ	fixedValue (0.375 m^2/s^2)	zeroGradient	zeroGradient	kqRWallFunction
ϵ	fixedValue (23.8 m^2/s^3)	zeroGradient	zeroGradient	epsilonWallFunction
ω	fixedValue (705.8 s^{-1})	zeroGradient	zeroGradient	omegaWallFunction

References

[1] Peng B, Locascio M, Zapol P, Li S, Mielke SL, Schatz GC, et al. Measurements of near-ultimate strength for multiwalled carbon nanotubes and irradiation-induced crosslinking improvements. Nat Nanotechnol 2008;3:626–31. https://doi.org/10.1038/nnano.2008.211.

[2] Luo J, Wang J, Bitzek E, Huang JY, Zheng H, Tong L, et al. Size-dependent brittle-to-ductile transition in silica glass nanofibers. Nano Lett 2016;16:105–13. https://doi.org/10.1021/acs.nanolett.5b03070.

[3] Papkov D, Zou Y, Andalib MN, Goponenko A, Cheng SZD, Dzenis YA. Simultaneously strong and tough ultrafine continuous nanofibers. ACS Nano 2013;7:3324–31. https://doi.org/10.1021/nn400028p.

[4] Dzenis Y. Structural nanocomposites. Science 2008;319:419–20. https://doi.org/10.1126/science.1151434 (80-).

[5] González C, Vilatela JJ, Molina-Aldareguía JM, Lopes CS, Llorca J. Structural composites for multifunctional applications: current challenges and future trends. Prog Mater Sci 2017;89:194–251. https://doi.org/10.1016/j.pmatsci.2017.04.005.

[6] Ritchie RO. The conflicts between strength and toughness. Nat Mater 2011;10:817–22. https://doi.org/10.1038/nmat3115.

[7] Rawal A, Mukhopadhyay S. Melt spinning of synthetic polymeric filaments. Advances in Filament Yarn Spinning of Textiles and Polymers. Cambridge, UK: Woodhead Publishing; 2014. p. 75–99.

[8] Wallenberger FT, Wallenberger FT, Bingham PA. Commercial and experimental glass fibers. editors. Fiberglass glass technology energy-friendly compositions and applications. New York: Springer US; 2010. p. 3–90. https://doi.org/10.1007/978-1-4419-0736-3_1.

[9] Kenry LCT. Nanofiber technology: current status and emerging developments. Prog Polym Sci 2017;70:1–17. https://doi.org/10.1016/j.progpolymsci.2017.03.002.

[10] Thenmozhi S, Dharmaraj N, Kadirvelu K, Kim HY. Electrospun nanofibers: new generation materials for advanced applications. Mater Sci Eng B Solid State Mater Adv Technol 2017;217:36–48. https://doi.org/10.1016/j.mseb.2017.01.001.

[11] Persano L, Camposeo A, Tekmen C, Pisignano D. Industrial upscaling of electrospinning and applications of polymer nanofibers: a review. Macromol Mater Eng 2013;298:504–20. https://doi.org/10.1002/mame.201200290.

[12] Drabek J, Zatloukal M. Meltblown technology for production of polymeric microfibers/nanofibers: a review. Phys Fluids 2019;31. https://doi.org/10.1063/1.5116336.

[13] Kellie G. Introduction to technical nonwovens. Kellie G., editor. Advance technology nonwovens. Elsevier; 2016. p. 1–17. https://doi.org/10.1016/B978-0-08-100575-0.00001-2.

[14] Ellison CJ, Phatak A, Giles DW, Macosko CW, Bates FS. Melt blown nanofibers: fiber diameter distributions and onset of fiber breakup. Polymer 2007;48:3306–16. https://doi.org/10.1016/j.polymer.2007.04.005 (Guildf).

[15] Soltani I, Macosko CW. Influence of rheology and surface properties on morphology of nanofibers derived from islands-in-the-sea meltblown nonwovens. Polymer 2018;145:21–30. https://doi.org/10.1016/j.polymer.2018.04.051 (Guildf).

[16] Majumdar B, Shambaugh RL. Air drag on filaments in the melt blowing process. J Rheol 1990;34:591–601. https://doi.org/10.1122/1.550097 (N Y N Y).

[17] Rao RS, Shambaugh RL. Vibration and stability in the melt blowing process. Ind Eng Chem Res 1993;32:3100–11. https://doi.org/10.1021/ie00024a020.

[18] Krutka HM, Shambaugh RL, Papavassiliou DV. Analysis of a melt-blowing die: comparison of CFD and experiments. Ind Eng Chem Res 2002;41:5125–38. https://doi.org/10.1021/ie020366f.

[19] Foley KA, Shambaugh RL. Fiber spinning with airfields enhanced by airfoil louvers. Text Res J 2019;89:3150–8. https://doi.org/10.1177/0040517518807444.

[20] Entov VM, Yarin AL. The dynamics of thin liquid jets in air. J Fluid Mech 1984;140:91–111. https://doi.org/10.1017/S0022112084000525.

[21] Chen T, Huang X. Air drawing of polymers in the melt blowing nonwoven process: mathematical modelling. Model Simul Mater Sci Eng 2004;12:381–8. https://doi.org/10.1088/0965-0393/12/3/002.

[22] Sun YF, Liu BW, Wang XH, Zeng YC. Air-flow field of the melt-blowing slot die via numerical simulation and multiobjective genetic algorithms. J Appl Polym Sci 2011;122:3520–7. https://doi.org/10.1002/app.34760.

[23] Hassan MA, Anantharamaiah N, Khan SA, Pourdeyhimi B. Computational fluid dynamics simulations and experiments of meltblown fibrous media: new die designs to enhance fiber attenuation and filtration quality. Ind Eng Chem Res 2016;55:2049–58. https://doi.org/10.1021/acs.iecr.5b04020.

[24] Wieland M, Arne W, Marheineke N, Wegener R. Melt-blowing of viscoelastic jets in turbulent airflows: stochastic modeling and simulation. Appl Math Model 2019;76:558–77. https://doi.org/10.1016/j.apm.2019.06.023.

[25] Sinha-Ray S, Yarin AL, Pourdeyhimi B. Meltblowing: i-basic physical mechanisms and threadline model. J Appl Phys 2010;108:034912. https://doi.org/10.1063/1.3457891.

[26] Xie S, Han W, Xu X, Jiang G, Shentu B. Lateral diffusion of a free air jet in slot-die melt blowing for microfiber whipping. Polymers 2019;11:1–14. https://doi.org/10.3390/polym11050788 (Basel).

[27] Yang Y, Huang H, Zeng Y. Turbulence of melt-blowing airflow field: comparison of a convergent jet and a typical free jet. Phys Fluids 2021;33. https://doi.org/10.1063/5.0055571.

[28] Hao X, Zeng Y. A review on the studies of air flow field and fiber formation process during melt blowing. Ind Eng Chem Res 2019;58:11624–37. https://doi.org/10.1021/acs.iecr.9b01694.

[29] Tan DH, Herman PK, Janakiraman A, Bates FS, Kumar S, Macosko CW. Influence of Laval nozzles on the air flow field in melt blowing apparatus. Chem Eng Sci 2012;80:342–8. https://doi.org/10.1016/j.ces.2012.06.020.

[30] Blim A, Jarecki L, Blonski S. Modeling of pneumatic melt drawing of polypropylene super-thin fibers in the Laval nozzle. Bull Pol Acad Sci Tech Sci 2014;62:43–54. https://doi.org/10.2478/bpasts-2014-0005.

[31] Yang Y, Zeng Y. Simultaneous measurement in nonisothermal melt-blowing airflow field: time-averaged and turbulent characteristics. Ind Eng Chem Res 2020;59:10664–72. https://doi.org/10.1021/acs.iecr.0c01278.

[32] Sun G, Han W, Wang Y, Xin S, Yang J, Zou F, et al. Overview of the fiber dynamics during melt blowing. Ind Eng Chem Res 2022;61:1004–21. https://doi.org/10.1021/acs.iecr.1c03972.

[33] Andreopoulos Y, Agui JH, Briassulis G. Shock Wave—Turbulence Interactions. Annu Rev Fluid Mech 2000;32:309–45. https://doi.org/10.1146/annurev.fluid.32.1.309.

[34] Merzkirch W. Optical Flow visualization. 3 -. 2nd ed. San Diego: Academic Press; 1987. p. 115–231. https://doi.org/10.1016/B978-0-08-050658-6.50007-2. flow vis.

[35] Quintero F, Penide J, Riveiro A, del Val J, Comesaña R, Lusquiños F, et al. Continuous fiberizing by laser melting (Cofiblas): production of highly flexible glass nanofibers with effectively unlimited length. Sci Adv 2020;6:eaax7210. https://doi.org/10.1126/sciadv.aax7210.

[36] Quintero F, Pou J, Comesaña R, Lusquiños F, Riveiro A, Mann AB, et al. Laser spinning of bioactive glass nanofibers. Adv Funct Mater 2009;19:3084–90. https://doi.org/10.1002/adfm.200801922.

[37] Quintero F, Dieste O, Pou J, Lusquiños F, Riveiro A. On the conditions to produce micro- and nanofibres by laser spinning. J Phys D Appl Phys 2009;42:065501. https://doi.org/10.1088/0022-3727/42/6/065501.

[38] Yang C, Jiang X, Gao X, Wang H, Li L, Hussain N, et al. Saving 80% polypropylene in facemasks by laser-assisted melt-blown nanofibers. Nano Lett 2022;22:7212–9. https://doi.org/10.1021/acs.nanolett.2c02693.

[39] Shapiro AH, Edelman GM. Method of characteristics for two-dimensional supersonic flow—graphical and numerical procedures. J Appl Mech 1947;14:A154–62. https://doi.org/10.1115/1.4009667.

[40] Duran I, Moreau S. Solution of the quasi-one-dimensional linearized Euler equations using flow invariants and the Magnus expansion. J Fluid Mech 2013;723:190–231. https://doi.org/10.1017/jfm.2013.118.

[41] Volkov YS, Galkin VM. On the choice of approximations in direct problems of nozzle design. Comput Math Math Phys 2007;47:882–94. https://doi.org/10.1134/S0965542507050119.

[42] Galkin V. Supersonic nozzle design. Tomsk Polytech Univ; 2011. https://portal.tpu.ru/SHARED/v/VLG/eng/Tab (accessed May 18, 2021).

[43] Otto A, Schmidt M. Towards a universal numerical simulation model for laser material processing. Phys. Procedia 2010;5:35–46. https://doi.org/10.1016/j.phpro.2010.08.120.

[44] Otto A, Vázquez RG. Fluid dynamical simulation of high speed micro welding. J Laser Appl 2018;30:32411. https://doi.org/10.2351/1.5040652.

[45] Darwish M, Orazi L, Angeli D. Simulation and analysis of the jet flow patterns from supersonic nozzles of laser cutting using OpenFOAM. Int J Adv Manuf Technol 2019;102:3229–42. https://doi.org/10.1007/s00170-019-03346-5.

[46] Darwish M, Orazi L, Reggiani B. Numerical analysis of the gas-assisted laser cutting flow from various supersonic nozzles. J Manuf Process 2020;56:382–9. https://doi.org/10.1016/j.jmapro.2020.04.037.

[47] Weller HG, Tabor G, Jasak H, Fureby C. A tensorial approach to computational continuum mechanics using object-oriented techniques. Comput Phys 1998;12:620–31. https://doi.org/10.1063/1.168744.

[48] Issa RI. Solution of the implicitly discretised fluid flow equations by operator-splitting. J Comput Phys 1986;62:40–65. https://doi.org/10.1016/0021-9991(86)90099-9.

[49] Kurganov A, Noelle S, Petrova G. Semidiscrete central-upwind schemes for hyperbolic conservation laws and hamilton – jacobi equations. SIAM J Sci Comput 2001;23:707–40. https://doi.org/10.1137/S1064827500373413.

[50] Greenshields CJ, Weller HG, Gasparini L, Reese JM. Implementation of semi-discrete, non-staggered central schemes in a colocated, polyhedral, finite volume framework, for high-speed viscous flows. Int J Numer Methods Fluids 2010;63:1–21. https://doi.org/10.1002/fld.2069.

[51] Bondarev AE, Kuvshinnikov AE, Shi Y, Fu H, Tian Y, Krzhizhanovskaya VV, Lees MH, Dongarra J, et al. Analysis of the accuracy of openfoam solvers for the problem of supersonic flow around a cone. In: Proceedings of the Computational Science – ICCS. Springer International Publishing; 2018. p. 221–30. editors2018.

[52] Kraposhin M, Bovtrikova A, Strijhak S. Adaptation of kurganov-tadmor numerical scheme for applying in combination with the PISO method in numerical simulation of flows in a wide range of mach numbers. Procedia Comput Sci 2015;66:43–52. https://doi.org/10.1016/j.procs.2015.11.007.

[53] Kraposhin MV, Banholzer M, Pfitzner M, Marchevsky IK. A hybrid pressure-based solver for nonideal single-phase fluid flows at all speeds. Int J Numer Methods Fluids 2018;88:79–99. https://doi.org/10.1002/fld.4512.

[54] Lastiwka D, Korobenko A, Johansen CT. Validation and verification of pimpleCentralFOAM and a 1D-ERAM Solver for analysis of an ejector-ramjet. In: Proceedings of the AIAA AVIATION forum. Il: American Institute of Aeronautics and Astronautics, Inc.; 2022. p. 3347. https://doi.org/10.2514/6.2022-3347.

[55] Schnars U, Jüptner WPO. Digital recording and numerical reconstruction of holograms. Meas Sci Technol 2002;13:R85–101. https://doi.org/10.1088/0957-0233/13/9/201.

[56] Kakue T, Yonesaka R, Tahara T, Awatsuji Y, Nishio K, Ura S, et al. High-speed phase imaging by parallel phase-shifting digital holography. Opt Lett 2011;36:4131–3. https://doi.org/10.1364/OL.36.004131.

[57] Desse JM, Picart P. Quasi-common path three-wavelength holographic interferometer based on Wollaston prisms. Opt Lasers Eng 2015;68:188–93. https://doi.org/10.1016/j.optlaseng.2014.12.018.
[58] Olchewsky F, Champagnat F, Desse JM. Multidirectional holographic interferometer for 3D gas density reconstruction. Imaging applied optics 2018 (3D, AO, AIO, COSI, DH, IS, LACSEA, LS&C, MATH, pcAOP). Optica Publishing Group; 2018. p. 3W5G.4. https://doi.org/10.1364/3D.2018.3W5G.4.
[59] Doval ÁF, Trillo C, Slangen P, Cerruti C. Hybrid optonumerical quasi Fourier transform digital holographic camera. editors. Speckle06 speckles, from grains to flowers, 6341. SPIE; 2006. p. 217–22. https://doi.org/10.1117/12.695340.
[60] Vest CM. Transparent objects: fringe interpretation, special techniques, and applications. Holographic interferometry. New York: John Wiley & Sons; 1979. p. 311–86.
[61] Fukuda T, Wang Y, Xia P, Awatsuji Y, Kakue T, Nishio K, et al. Three-dimensional imaging of distribution of refractive index by parallel phase-shifting digital holography using Abel inversion. Opt Express 2017;25:18066–71. https://doi.org/10.1364/OE.25.018066.
[62] Ciddor PE. Refractive index of air: new equations for the visible and near infrared. Appl Opt 1996;35:1566–73. https://doi.org/10.1364/AO.35.001566.
[63] Picard A, Davis RS, Gläser M, Fujii K. Revised formula for the density of moist air (CIPM-2007). Metrologia 2008;45:149–55. https://doi.org/10.1088/0026-1394/45/2/004.
[64] Lanen TAWM. Digital holographic interferometry in flow research. Opt Commun 1990;79:386–96. https://doi.org/10.1016/0030-4018(90)90089-C.
[65] Smithey WJH. Value of mach angle for a given prandtl-meyer angle. AIAA J 1974; 12:1596–7. https://doi.org/10.2514/3.49553.
[66] Jaunet V, Arbos S, Lehnasch G, Girard S. Wall pressure and external velocity field relation in overexpanded supersonic jets. AIAA J 2017;55:4245–57. https://doi.org/10.2514/1.J055874.
[67] Erengil ME, Dolling DS. Unsteady wave structure near separation in a Mach 5 compression rampinteraction. AIAA J 1991;29:728–35. https://doi.org/10.2514/3.10647.
[68] Clemens NT, Narayanaswamy V. Low-frequency unsteadiness of shock wave/turbulent boundary layer interactions. Annu Rev Fluid Mech 2014;46:469–92. https://doi.org/10.1146/annurev-fluid-010313-141346.
[69] Sasaki K, Barros DC, Cavalieri AVG, Larchevêque L. Causality in the shock wave/turbulent boundary layer interaction. Phys Rev Fluids 2021;6:064609. https://doi.org/10.1103/PhysRevFluids.6.064609.
[70] Shinde V, McNamara J, Gaitonde D, Barnes C, Visbal M. Transitional shock wave boundary layer interaction over a flexible panel. J Fluids Struct 2019;90:263–85. https://doi.org/10.1016/j.jfluidstructs.2019.07.007.
[71] Boyer NR, McNamara JJ, Gaitonde DV, Barnes CJ, Visbal MR. Features of panel flutter response to shock boundary layer interactions. J Fluids Struct 2021;101: 103207. https://doi.org/10.1016/j.jfluidstructs.2020.103207.
[72] Penide J, Quintero F, Fernández JL, Fernández-Arias M, Barciela R, del Val J, et al. Anamorphic beam shaping system designed to optimize irradiance distribution in the Cofiblas process for glass nanofibers production. Opt Lasers Eng 2022;152: 106972. https://doi.org/10.1016/j.optlaseng.2022.106972.